# Integration of a photocatalytic multi-tube reactor for indoor air purification in HVAC systems : a feasibility study

# Integration of a photocatalytic multi-tube reactor for indoor air purification in HVAC systems: a feasibility study

*Jeroen van Walsem[†‡], Jelle Roegiers[†‡], Bart Modde[§], Silvia Lenaerts[†], Siegfried Denys[†,*]*

† Sustainable Energy, Air & Water Technology, Department of Bioscience Engineering, University of Antwerp, Groenenborgerlaan 171, B-2020 Antwerp, Belgium.

§ Vento Ltd., Bedrijvenpark Coupure 5, B-9700 Oudenaarde, Belgium.

* E-mail: Siegfried.Denys@uantwerp.be

Fax: +32 3 265 32 25. Tel: +32 3 265 32 30.

‡ These authors contributed equally.

**Keywords**

HVAC; Indoor air; Permeability; Photocatalysis; VOC

**Highlights**

- Substrates for PCO-reactors in ventilation systems were selected based on permeability and exposed surface area
- In-depth characterization of coated glass tubes as suitable substrate for PCO
- High acetaldehyde conversion efficiencies are shown at a range of operating conditions
- The feasibility of the technology for HVAC applications was validated in an air-tight climate chamber

# 1. Abstract

This work is focused on an in-depth experimental characterization of multi-tube reactors for indoor air purification integrated in ventilation systems. Glass tubes were selected as an excellent photocatalyst substrate to meet the challenging requirements of the operating conditions in a ventilation system in which high flow rates are typical. Glass tubes show a low pressure drop which reduces the energy demand of the ventilator and additionally, they provide a large exposed surface area to allow interaction between indoor air contaminants and the photocatalyst. Furthermore, the performance of a range of P25 loaded sol-gel coatings was investigated, based on their adhesion properties and photocatalytic activities. Moreover, the UV light transmission and photocatalytic reactor performance under various operating conditions were studied. These results provide vital insights for the further development and scaling up of multi-tube reactors in ventilation systems which can provide a better comfort, improved air quality in indoor environments and reduced human exposure to harmful pollutants.

# 2. Introduction

Indoor air quality (IAQ) has become of vital importance to health globally – especially in the developed countries where people generally spend more than 80% of their time in an indoor environment e.g. at home, school, office, public buildings and gyms (Ao and Lee 2005; Bourgeois et al. 2012). Many volatile organic compounds (VOCs) have been identified indoors which are hazardous substances emitted from construction materials, indoor equipment or human indoor activities such as cooking or heating (Yu and Brouwers 2009; Sanchez et al. 2012). VOCs may trigger the sick building syndrome (SBS), which covers the broad range of health problems caused by bad IAQ (Auvinen and Ã 2008; Mo et al. 2009a). Nowadays, ventilation systems D (balanced ventilation) are commonly used to maintain the indoor air quality. These systems are automatically controlled by mechanical air supply and exhaust

through fans. A network of pipes throughout the building supplies fresh air in each room. The main disadvantages of these systems include the high energy consumption of the fans, heat losses and the dependency on the outdoor air quality (OAQ). To ensure a healthy IAQ, an interesting strategy is to combine ventilation and air purification (Zhang et al. 2003). Of the advanced air purification methods, photocatalytic oxidation (PCO) is a promising technique for integration into heating, ventilation and air conditioning (HVAC) systems (Zhao and Yang 2003; Mo et al. 2009b; Paz 2010; Destaillats et al. 2012). PCO technology exposes a catalyst, mostly titanium dioxide $TiO_2$, to ultraviolet (UV-A) light to produce hydroxyl radicals and superoxide anions (Mills and Hunte 2000). These radicals are extremely reactive and are able to mineralize VOCs into $H_2O$ and $CO_2$. The advantage of using an air purification device is that the IAQ can be maintained with a minimum of ventilation, resulting in less energy consumption and even a contribution to a better OAQ. PCO is an interesting, cost-effective and efficient approach for indoor air pollution abatement (Sleiman et al. 2009) but its commercialization is delayed by the many requirements of a PCO device or reactor and the substrate for the photocatalyst. Indeed, integration or retrofitting of a PCO device into a HVAC system requires special features to deal with the typical high flow rates. The photocatalytic substrate must allow the contaminated air to pass through with a minimal pressure drop, permit sufficient contact time between VOC and photocatalyst, have a high surface area available for coating with excellent adherence and be permeable for UV light (Zhao and Yang 2003; Zhong and Haghighat 2015). Numerous substrates have been proposed in the literature, such as glass fibers, glass beads, optical fibers, ceramic honeycomb monoliths or stainless steel (Wang et al. 1998; Hossain et al. 1999; Sun et al. 2000; Chen and Dionysiou 2006; Bourgeois et al. 2012; Verbruggen et al. 2016). In previous work, we presented borosilicate glass tubes as a substrate with demonstrated high efficiency toward the degradation of acetaldehyde in air (van Walsem et al. 2016). The choice of glass tubes was mainly based on intuitive reasoning and convenience:

they can easily be coated and packed to constitute a transparent monolith-like multi-tube reactor, aligned with the air flow to minimize the pressure drop. Moreover, borosilicate glass is relatively cheap and has excellent UV-A light transmitting properties. The aim of previous research was to derive all photocatalytic relevant kinetic parameters of one particular photocatalytic reactor, i.e. the multi-tube reactor, using a modelling approach for design and scaling up purposes. In this work we present a more in-depth characterization of borosilicate glass tubes as a suitable substrate and optimized substrate for its specified application, including a more reasoned, quantitative comparison with other convenient substrates. Based on earlier research, two additional potential substrates were selected for their excellent UV-A light transmission properties: borosilicate glass beads which additionally showed good coating and photocatalytic properties (Verbruggen et al. 2011), and glass fiber mats because of their open structure provided by the long, thin fibers (Verbruggen et al. 2016). We will show that glass tubes have some important advantages for ventilation applications, especially in terms of pressure drop and exposed surface area. Moreover, various P25 loaded sol-gel coatings were investigated under different operating conditions, i.e. pollutant concentrations, flow rates and UV-A light irradiance. It is shown that a case-by-case approach is required to optimize the multi-tube reactor for HVAC applications, as its performance highly depends on the operating conditions of the system.

# 3. Methodology

## 3.1 Selection of glass tubes as a suitable substrate: permeability and exposed surface area

A suitable photocatalyst substrate for a PCO reactor integrated in a HVAC system should exhibit a minimum pressure drop caused by friction losses. Pressure losses increase the energy demand and can cause malfunction of the ventilation fan and thus undermine the proper functioning of the ventilation system. The main challenge is to select a substrate that is 'open' enough to limit the pressure loss but at the same time provides a large exposed surface area to allow interaction

between contaminant and photocatalyst to achieve complete mineralization. For these reasons, the permeability and exposed surface area were chosen as main selection criteria. Three candidate substrates were tested and compared: borosilicate glass tubes, borosilicate glass beads and glass fibers mats. The glass tubes had an internal diameter of 5, 7 and 9 mm and an external diameter of 7, 9 and 11 mm respectively; they are further described as 5ID7ED, 7ID9ED and 9ID11ED. Glass beads of two sizes (diameter 14 mm and 16 mm) were used. Commercial glass fibers mats were selected (Profil, 2.PS3"B.050) consisting of fibers with a thickness of (36 ± 7) µm, determined by at least 30 thickness measurements of different fibers by optical microscopy (Verbruggen et al. 2016). They form a structure with large open pores and the density can be adapted by compression. Glass fibers with three different densities (0.0054 g/cm³, 0.0090 g/cm³ and 0.0124 g/cm³) were used in this study.

3.1.1. Pressure losses and permeability tests

Pressure losses over the three substrates were measured and compared in a reactor integrated in a closed circuit air duct system. The setup consisted of circular pipes (inner diameter 10.3 cm) with a total length of 600 cm. Air movement was created by a controllable inline duct fan which could induce air flow velocities varying from 1.14 m/s to 4.4 m/s (for an empty reactor). The fan curve (pressure difference over the fan versus flow rate) was provided by the manufacturer. The reactor section consisted of a transparent pipe (length 54.5 cm, inner diameter 11.4 cm) that was fitted in the closed circuit. In order to compare the substrates, the reactor was partially (over a length of 20 cm) filled with glass tubes, glass beads or glass fibers and the pressure drop was measured by a differential pressure sensor (DPS) consisting of a pressure module (Fluke 717 30G, Fluke Corp.) with a range of -83 to 206.84 kPa and a pressure calibrator (Fluke 700PD2, Fluke Corp.). In order to keep the glass beads packed in the reactor, sparse polylactic acid grids (created with a 3D printer) were used on both sides of the beads. The presence of the grids required a small correction for the additional pressure drop. Air flow rate was measured

120 at 20 cm before the reactor inlet by a hotwire air velocity sensor (CTV 110, KIMO instruments).
121 In order to quantitatively compare the 'openness' of the substrates, measurements of the
122 pressure drop were performed at a range of air flow velocities depending on the flow resistance
123 of the substrate (determined by the fan curve of the duct fan) and the experimental results were
124 correlated to the Darcy-Forchheimer law by regression to obtain their permeability κ ($m^2$).
125 Darcy's law is a simple proportional relationship between the instantaneous discharge rate for
126 a single-phase flow in a porous medium; in the Darcy-Forchheimer law, the Forchheimer term
127 accounts for the non-linear behavior (influence of kinetic energy and inertia) of the pressure
128 drop as a function of flow speed (Bejan 2013) (Eq. 1):

$$\frac{\Delta P}{\Delta x} = -\frac{\mu}{\kappa} \times q - \frac{(\rho \times q^2)}{\kappa_1} \qquad \text{(Eq. 1)}$$

129 with $\Delta P$ the pressure drop (Pa), $\Delta x$ the length of the substrate in the flow direction (m), $\mu$ the
130 viscosity of the flow (Pa.s), $q$ the flow speed (m/s), $\rho$ the density ($kg/m^3$) and $\kappa_I$ the inertial
131 permeability (m).

132 3.1.2. Exposed surface area

133 The exposed surface area of the three substrates was determined from simple geometrical
134 calculations, considering a filled test reactor (11.4 cm diameter, 20 cm length) with glass tubes,
135 glass beads and glass fibers. The reactor filled with 5ID7ED, 7ID9ED and 9ID11ED glass tubes
136 resulted in respectively 190, 113 and 77 tubes. In case of glass beads, the densest packing
137 corresponded to 513 beads (16 mm diameter) and 819 beads (14 mm diameter). The surface
138 area of glass fibers was calculated from the weight, the density of glass ($2.5 g/cm^3$) and the fiber
139 thickness of $36 \pm 7$ µm, determined by 30 optical microscopy measurements.

140 3.1.3 Pressure losses over glass tubes at realistic air speed

141 With the fan used in the experimental setup described in 3.1.1., we could only reach a maximum
142 air speed of 4.4 m/s for an empty reactor. In the ducts of a ventilation system, air speeds of up

to 7 m/s are no exception. In order to further characterize glass tubes in terms of their airflow resistance properties at more realistic (higher) air speeds, a modelling approach was used. An additional advantage of modelling is that also geometrical effects (other lengths and diameters of tubes) can easily be studied. The commercial software package Comsol Multiphysics v5.2a was used to perform computational fluid dynamics (CFD) simulations to accurately describe the fluid flow processes in the studied geometry. In Figure 1, the geometry of the reactor filled with 7ID9ED glass tubes was shown as example. Additionally, a cross section of the reactor and the mesh were given. To ensure mesh quality, a user-defined mesh, consisting of 868,655 tetrahedral and 743,600 prism elements was created with an average mesh quality of 0.72. The reactor, consisting of packed glass tubes, has the same dimensions as the one described in setup 3.1.1, i.e. 11.4 cm diameter with both 20 and 50 cm glass tube length. The approach for air flow modelling is similar to the one described in earlier research (Verbruggen et al. 2016). Except, in this work a turbulent air flow module was used to calculate the pressure drop caused by packed 5ID7ED, 7ID9ED and 9ID11ED glass tubes, (aligned with the air flow) at different inlet velocities, ranging from 1 to 7 m/s.

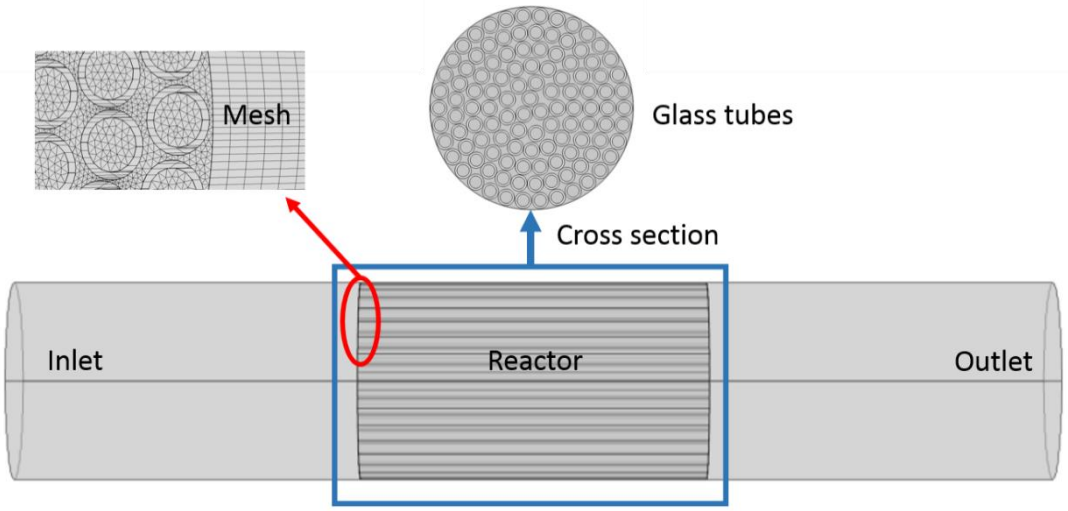


Figure 1: Comsol geometry for CFD simulations in a reactor filled with glass tubes, at different inlet velocities.

### 3.2 Selection of photocatalytic coating

Obviously, the photocatalytic coating is a significant and determining component of a PCO reactor. Considering the installation, maintenance and operating conditions (e.g. high wind speeds) of ventilation systems, excellent coating adhesion of the photocatalyst is also vital. A P25 based powder-modified sol-gel, proposed by Chen and Dionysiou (2006), was chosen for its excellent adhesion and good photocatalytic properties for borosilicate glass and stainless steel materials (Chen and Dionysiou 2006, 2008). We applied this method for glass tubes with a broad range of P25 loadings to compare adhesion properties and photocatalytic activity. The glass tubes were dip-coated (Bungard Elektronik, RDC21-K dipcoater) with a fixed withdrawal speed of 120 mm/min in P25 based powder-modified sol-gels, as described by the method of Chen and Dionysiou (2006) and afterwards dried in the oven at 90°C for 24 hours. The modified sol-gels consisted of a 0.5 M solution of commercial titanium isopropoxide (TTIP, 97 %, Aldrich), isopropanol (i-PrOH, Sigma- Aldrich) and diethanolamine (DEA, Sigma-Aldrich) (with a DEA/TTIP molar ratio of 4 and a $H_2O$/TTIP molar ratio of 2) and P25 $TiO_2$ (Evonik) at seven different loadings: 0 g/L, 1 g/L, 5 g/L, 10 g/L, 30 g/L, 50 g/L and 70 g/L. The coating procedure requires a subsequent calcination step at 500°C (Chen and Dionysiou 2006). For each coating, the adhesion of catalyst particles to the substrate was evaluated by means of the classic scotch tape test (Chen and Dionysiou 2007), and by submitting the coated substrate to parallel compressed airflow, corresponding to a wind speed of at least 13 m/s as measured by a hotwire air velocity sensor (CTV 110, KIMO instruments) while monitoring the amount of released nanoparticles, using an ultrafine particle counter (P-trak, TSI systems).

The photocatalytic activities of the seven P25 based powder-modified sol-gels were tested according to ISO 22197-2:2011, a standard performance test method of semi-conductive photocatalytic materials for the removal of acetaldehyde in air (Mills et al. 2012). The experiments were performed with a fully automated setup which is described in detail by Tytgat

187 *et al.* (Tytgat et al. 2012). Acetaldehyde (Messer, 1% in N2) was mixed with synthetic clean air
188 (Messer) with a fixed total flow rate of 1,000 $cm^3$/min, resulting in a stable continuous flow of
189 $2 \times 10^{-4}$ mol/$m^3$ acetaldehyde (~5 ppmv). A specified relative humidity of 50% was obtained
190 using a temperature-controlled gas wash bottle. The reactor can be by-passed to force the
191 contaminated gas flow directly to the measurement devices. The outlet acetaldehyde
192 concentration was measured every 4 minutes using a Compact GC 4.0 analyser (Interscience)
193 equipped with a flame ionization detector (FID). The photocatalytic ISO standard reactor
194 (Figure 2) was made from stainless steel, which is inert with regard to acetaldehyde and UV
195 light. The test samples were illuminated through a quartz glass window resulting in an incident
196 UV (300-400 nm) irradiance of 1,000 µW/$cm^2$. Prior to each photocatalytic experiment, the
197 samples were pretreated for 24 hours with UV-A light of an incident light irradiance of 1,500
198 µW/$cm^2$ to remove all organic residues. Borosilicate test samples (glass plates 20 cm length
199 and 10 cm width) were coated using the modified sol-gel method with 4 different P25 loadings,
200 i.e. 30 g/L, 50 g/L, 70 g/L and 100 g/L. Photocatalytic activity experiments were performed in
201 three phases: (1) 30 minutes in by-pass mode during which the gas flow is sent directly to the
202 GC-FID without passing through the reactor, in order to verify if the initial concentration level
203 of acetaldehyde is stable and fixed at $2 \times 10^{-4}$ mol/$m^3$, (2) 90 minutes of adsorption phase where
204 the gas flows through the ISO standard reactor in order to achieve adsorption-desorption
205 equilibrium and (3) 180 minutes of photocatalytic phase where gas flow through the reactor
206 under UV-A illumination.

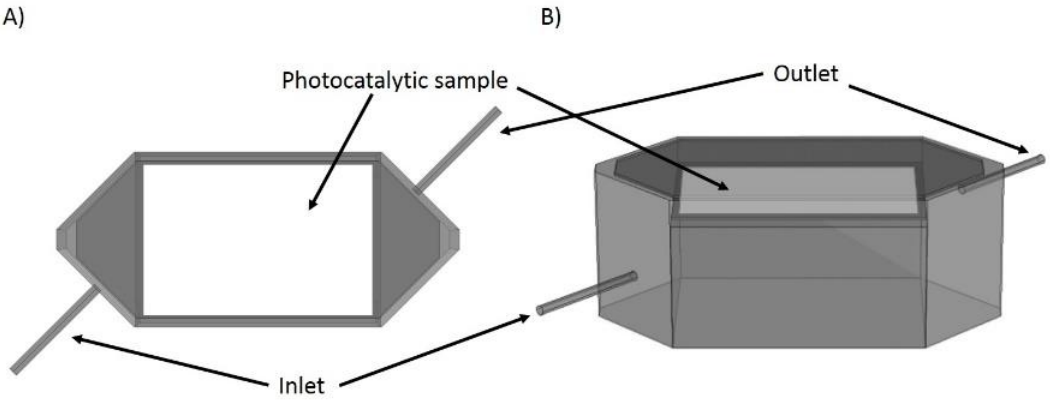


Figure 2: ISO standard reactor; A) top view; B) side view.

The photocatalytic activities of the coatings were expressed and compared by common-used expressions from the literature (Mills et al. 2012; Claudio et al. 2013): the removal percentage of acetaldehyde $R_A$ [%] (Eq. 2), the quantity of acetaldehyde removed during the whole experiment $n_A$ [µmol] (Eq. 3), the quantity of acetaldehyde removed during the last hour of the experiment $n_A(60)$ [µmol] (Eq. 4) and the photocatalytic rate per unit area $r$ [µL/min.m²] (Eq. 5).

$$R_A = \frac{\phi_{AO} - \phi_A}{\phi_{AO}} \times 100 \quad \text{(Eq. 2)}$$

$$n_A = \left(\frac{60f}{22.4}\right) \times B \quad \text{(Eq. 3)}$$

$$n_A(60) = \left(\frac{60f}{22.4}\right) \times (\phi_{AO} - \phi_A) \quad \text{(Eq. 4)}$$

$$r = \frac{\phi_{AO} \times f}{S} \times log\left(\frac{1}{1 - \frac{\phi_A}{\phi_{A0}}}\right) \quad \text{(Eq. 5)}$$

where $\phi_{AO}$ is the supply volume fraction of acetaldehyde [ppm], $\phi_A$ the volume fraction of acetaldehyde at the reactor outlet [ppm], $f$ the flow rate of test gas [L/min], $B$ the amount of acetaldehyde removed [ppm/h] and $S$ the surface area of the sample exposed to light [m²].

## 3.3 Reactor performance

Based on the results of the comparative study of candidate substrates, a laboratory scale PCO reactor was constructed from glass tubes as shown in Figure 3. The reactor consisted of a borosilicate glass tube with an internal diameter of 29 mm and a length of 44 cm, provided with inlet and outlet connections (diameter 4 mm) perpendicular to its longitudinal axis and a closing mechanism using butyl rubbers to seal both ends airtight. The test reactor was symmetrically filled with 7 coated glass tubes (7ID9ED) to from a 'multi-tube reactor'. Two 25 W UV-A lamps (Philips) were positioned on opposite sides and parallel to the reactor, at a distance of 2.5 cm from the reactor housing and resulting in an incident irradiance on both outer surfaces of the reactor of 2.1 mW $cm^{-2}$, as measured by a calibrated Avantes Avaspec-3648 spectrometer (see further).

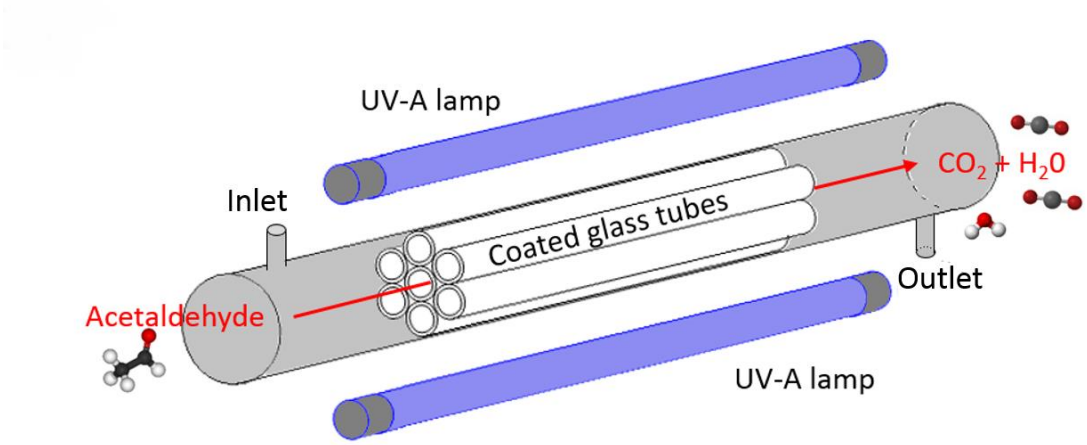


Figure 3: Lab-scale Multi-Tube reactor.

3.3.1 Light irradiance measurements

Light irradiance and uniformity are among the critical performance parameters of a PCO reactor, especially when high airflow rates are involved. 'Dark spots' should be avoided as they can severely limit the photocatalytic conversion efficiency (Sopyan et al. 1996; Brosillon et al. 2008). Light irradiance and uniformity are determined by the light source but also by the properties of the reactor geometry, the substrate and the coating. A calibrated Avantes Avaspec-

3648 spectrometer was used to measure the emitted spectral UV light irradiance at several positions in the multi-tube reactor. The light irradiance measurements were integrated over the emitted spectral range (between 300 and 400 nm and a peak at 367 nm). For the light irradiance measurements, only one 25 W UV-A lamp (Philips) was used, positioned above and parallel to the reactor at a distance of 5 mm from the reactor. Based on the configuration of the glass tubes (7ID9ED), 4 incident light irradiance measurement positions were defined, as shown in Figure 4. Measurements were performed for uncoated tubes and for tubes coated with modified sol-gels prepared with 6 different P25 loadings: 0, 1, 5, 10, 30, 50 and 70 g/L. Each measurement was done with the sensor surface oriented perpendicular to the light source to measure the UV light extinction while travelling through different layers of tubes and coatings.

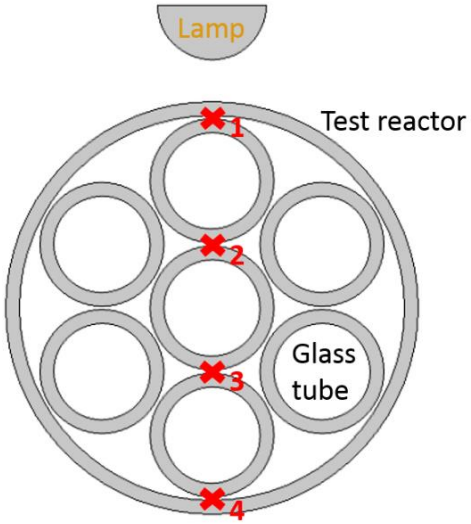


Figure 4: Light irradiance measurements at 4 fixed positions.

3.3.2 Reactor performance at low flow rates and high acetaldehyde concentrations

To evaluate the multi-tube reactor concept, activity measurements were performed with coatings prepared from 7 different P25 loadings (0, 1, 5, 10, 30, 50 and 70 g/L P25) and at two fixed inlet air velocities. Hereto, acetaldehyde (Messer, 1% in $N_2$) was mixed with synthetic clean air (Messer) using the fully automated test setup at a fixed total flow rate of 500 and 1,500

257 $cm^3$/min. In this case, the outlet acetaldehyde concentration was measured using online FTIR
258 spectroscopy by means of the IR peak height at 2728 $cm^{-1}$, corresponding to the *v*(C-H) stretch
259 vibration. Prior to these performance experiments, the coated substrates were irradiated by UV
260 light for 24 hours in order to clean all organic rest fractions from the $TiO_2$ surface. These
261 experiment were carried out using two 25 W UV-A lamps at a parallel distance of 25 mm to the
262 reactor housing, as shown in Figure 3. Activity and adsorption experiments were performed in
263 four phases: (1) 15 minutes in by-pass mode during which the gas flow is sent directly to the
264 FTIR detection cell without passing through the reactor, in order to determine the initial
265 concentration level of acetaldehyde, (2) 180 minutes of adsorption phase where the gas flows
266 through the reactor in dark conditions in order to achieve adsorption-desorption equilibrium
267 and thus to be able to calculate the adsorption capacity, (3) 90 minutes gas flow through the
268 reactor under UV-A illumination to determine the photocatalytic activity and (4) another
269 adsorption phase to re-establish the adsorption/desorption equilibrium in order to exclude the
270 occurrence of leaks in the reactor or MFC inaccuracy. The acetaldehyde adsorption capacities
271 of the 7 sets of coatings at equilibrium were derived by integrating the non-steady-state
272 acetaldehyde concentration over time during the adsorption phase, and subtracting the obtained
273 values from the amount of acetaldehyde entering the reactor during the same period
274 (Verbruggen et al. 2012). As in previous work, a correction was made for the dead space in the
275 reactor by performing the same experiments with 7 uncoated glass tubes at the same fixed flow
276 rate and bulk acetaldehyde concentration (van Walsem et al. 2016). For every experiment, the
277 acetaldehyde removal (%) was derived by the ratio of the steady-state acetaldehyde
278 concentration in phase 3 (UV-A illuminated conditions) to the steady-state acetaldehyde
279 concentration in phase 1.

280 3.3.3 Reactor performance at high flow rates and low acetaldehyde concentrations

As final validation, a multi-tube reactor was tested under realistic HVAC operating conditions in an airtight climate chamber, built in accordance with the AFNOR XP B44-013 standard (Kartheuser et al. 2012). The climate chamber was made of polymethyl methacrylate (PMMA) with an internal volume of 1.2 m³ and was equipped with two fans (Panasonic ASFN10392, 171 m³/h) to ensure air homogenization, a septum for acetaldehyde injection and an air-tight sealed PMMA cover to insert or remove the photocatalytic reactor. The Compact GC 4.0 analyser (Interscience) equipped with a flame ionization detector (FID) (as described in 3.2) was connected online with the climate chamber in order to automatically sample and analyze the acetaldehyde concentration once every 4 minutes. The experiments were carried out with an initial concentration of $2 \times 10^{-4}$ mol/m³ (~5 ppmv) and lasted until the lower detection limit of about $2 \times 10^{-5}$ mol/m³ (~0.5 ppmv) was reached. Prior to the photocatalytic experiments, a leak-test was performed by checking the stability of the acetaldehyde concentration in absence of the photocatalytic reactor. Again, each experiment was preceded by a cleaning phase in which the coating was irradiated by UV-A light for 24 hours. Based on the results of the reactor performance at low flow rates and high acetaldehyde concentration (3.3.2), 10, 30 and 50 g/L P25 based coatings were selected for these experiments. The reactor configuration is the same as described in 3.3.2 but in this case the lamps were positioned at a parallel distance of 5 mm from the reactor and the air flow was generated by a fan (Orion OD3010-12HB, 7.5 m³/h), positioned at the reactor outlet, resulting in an air flow velocity of about 2 - 2.5 m/s which corresponds to a passage through the reactor of 4 to 5 times the chamber volume per hour. The performance of the multi-tube reactors were quantitatively compared by calculating the Clean Air Delivery Rate (CADR) which represents the effective volume of cleaned air per hour (Costarramone et al. 2015) (Eq. 6):

$$\frac{dC}{dt} = -\left(\frac{CADR}{V}\right) \times C \qquad (Eq. 6)$$

where V is the volume of the air-tight chamber [m³], C the contaminant concentration inside the chamber at time *t* [mol/m³] and CADR the Clean Air Delivery Rate [m³/h].

# 4. Results and discussion

## 4.1 Selection of a suitable substrate

### 4.1.1 Permeability and exposed surface area

In Table 1, the permeability ($\kappa$) and inertial permeability ($\kappa_1$), calculated using the Darcy-Forcheimer law, and the exposed surface area of the studied substrates are shown. As mentioned, a suitable substrate combines a high permeability to minimize the energy consumption with a large exposed surface area available for coating. A plot of the exposed surface area against the permeability is shown in Figure 5. The most suitable substrate is located in the right upper corner of the figure, where the highest permeability and exposed surface area are combined. For each type of substrate, a trade-off exists between these two vital criteria as illustrated by the dashed trend lines plotted in Figure 5. The glass tubes scored best on both criteria which makes them the most suitable substrate for the application. Even though glass beads with large diameters were used to minimize the pressure drop, their permeability was still very low compared to the other substrates. Besides, their exposed surface area was relatively low. The glass fibers showed a moderate performance on both permeability and exposed surface area.

Table 1: An overview of the permeability, inertial permeability and exposed surface area.

| **Substrate** | **Permeability (m²)** | **Inertial permeability (m)** | **Exposed surface area (cm²/cm³)** |
|---|---|---|---|
| Glass fibers (0.0124 g/cm³) | $2.18 \times 10^{-7}$ ($\pm 1.35 \times 10^{-8}$) | $5.45 \times 10^{-2}$ ($\pm 6.23 \times 10^{-3}$) | 4.95 |
| Glass fibers (0.009 g/cm³) | $3.34 \times 10^{-7}$ ($\pm 8.75 \times 10^{-9}$) | $8.79 \times 10^{-2}$ ($\pm 1.80 \times 10^{-3}$) | 3.56 |
| Glass fibers (0.0054 g/cm³) | $7.36 \times 10^{-7}$ ($\pm 4.08 \times 10^{-9}$) | $9.66 \times 10^{-2}$ ($\pm 1.29 \times 10^{-3}$) | 2.14 |
| Glass beads (14 mm diameter) | $1.76 \times 10^{-8}$ ($\pm 6.21 \times 10^{-9}$) | $9.26 \times 10^{-4}$ ($\pm 1.39 \times 10^{-4}$) | 2.21 |

| | | | |
|---|---|---|---|
| Glass beads (16 mm diameter) | $6.84 \times 10^{-8}$ ($\pm 1.84 \times 10^{-8}$) | $6.43 \times 10^{-4}$ ($\pm 5.67 \times 10^{-5}$) | 1.81 |
| Glass tubes (5ID7ED) | $5.82 \times 10^{-7}$ ($\pm 7.90 \times 10^{-8}$) | $2.49 \times 10^{-2}$ ($\pm 5.78 \times 10^{-3}$) | 7.02 |
| Glass tubes (7ID9ED) | $9.14 \times 10^{-7}$ ($\pm 8.38 \times 10^{-8}$) | $4.52 \times 10^{-2}$ ($\pm 8.34 \times 10^{-3}$) | 5.57 |
| Glass tubes (9ID11ED) | $1.36 \times 10^{-6}$ ($\pm 8.21 \times 10^{-8}$) | $6.14 \times 10^{-2}$ ($\pm 3.26 \times 10^{-3}$) | 4.74 |

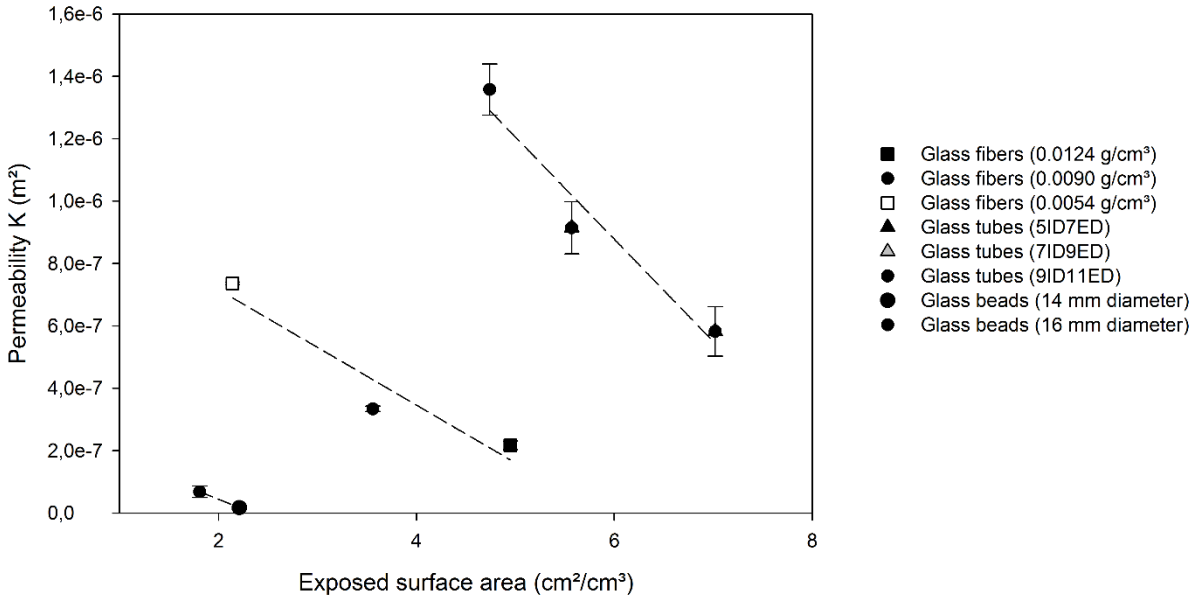


Figure 5: Permeability K ($m^2$) plotted against exposed surface area ($cm^2/cm^3$).

4.1.2 Pressure losses over glass tubes at realistic air speed

Figure 6 shows the pressure drop corresponding to 3 configurations of glass tubes (5ID7ED, 7ID9ED and 9ID11ED) as calculated by the Comsol model with a relative convergence error of $1 \times 10^{-3}$. The reported pressure drops are the modelled pressure differences between the actual locations of the DPS. Results are given for a completely stacked reactor, for air velocities ranging from 1 to 7 m/s (air velocity at the anemometer position). For each type of glass tubes, two glass tube lengths were considered: 20 and 50 cm. As a practical guideline based on energy consumption considerations, a threshold of 200 Pa was set for the additional pressure drop, caused by the reactor. All configurations of 20 cm length fulfil this requirement, except for 5ID7ED at a velocity of 7 m/s. For a reactor length of 50 cm, only the pressure loss corresponding to the largest diameter of tubes (9ID11ED) remains below the set point.

Obviously, the aerodynamic entry length (where the flow is developing) causes most of the pressure drop. The entry length depends on the flow characteristics (the Reynolds number) and the tube diameter. For many turbulent pipe or tube flows, the entry length $L$ is approximated as (Çengel et al. 2012) (Eq. 6):

$$L = 1.359\ \mathrm{Re}^{1/4} D \qquad \text{(Eq. 6)}$$

With $D$ the diameter of the glass tubes [m]. According to this formula, entry lengths for the tubes varied from 3 cm (smallest $D$ at the lowest velocity) to 11 cm for the case of largest $D$ at the highest velocity. As can be seen from the results, the pressure drop per unit length corresponding to tubes of 20 cm is at least a factor 1.45 higher than for tubes of 50 cm. From this point of view, it is better to extend the length of the reactor rather than using smaller tubes.

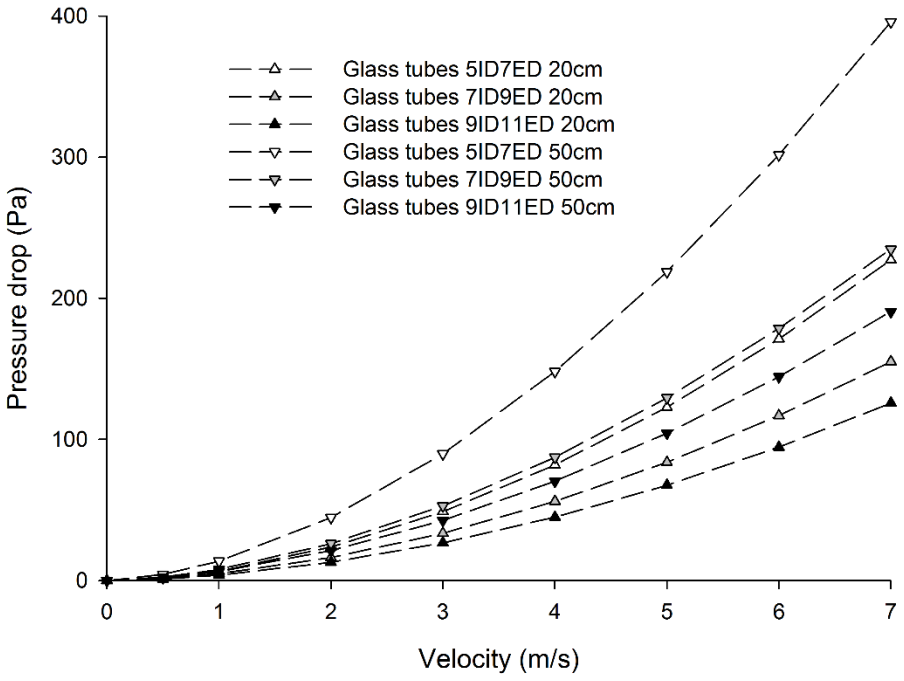


Figure 6: Pressure drop, calculated using a modelling approach, at realistic velocities (1-7 m/s).

## 4.2 Selection of photocatalytic coating

### 4.2.1 Coating adhesion

0-50 g/L P25 coatings passed the classic scotch tape test. For the 70 g/L P25 coating, a small amount of white titanium dioxide particles was released on the tape and the 100 g/L P25 coating completely failed the test, rendering it useless for the application considering the maintenance and installation of the reactor. For each P25 loaded sol-gel coating, the amount of released nanoparticles under compressed airflow equaled the background measurement. This proves that, once the coated glass tubes are immobilized in the ventilation system, it is suitable for its operating conditions in which high air flow velocities are typical.

### 4.2.2 Photocatalytic activity of the coating

Table 2: Quantitatively comparison of the photocatalytic activity of the coating.

| **Parameters** | **30 g/L** | **50 g/L** | **70 g/L** | **100 g/L** |
|---|---|---|---|---|
| nA (µmol) | 14.13 (± 2.2) | 17.46 (± 2.7) | 23.10 (± 3.6) | 25.61(± 3.9) |
| nA 60 (µmol) | 4.79 (± 0.73) | 5.76 (± 0.9) | 7.54 (± 1.2) | 8.23 (± 1.3) |
| RA (%) | 37.93 (± 5.8) | 45.89 (± 7.1) | 59.82 (± 9.2) | 66.07 (± 10.2) |
| r (µL/min.m²) | 112.45 (± 17.3) | 143.85 (± 22.1) | 214.62 (± 33.03) | 251.28 (± 38.7) |

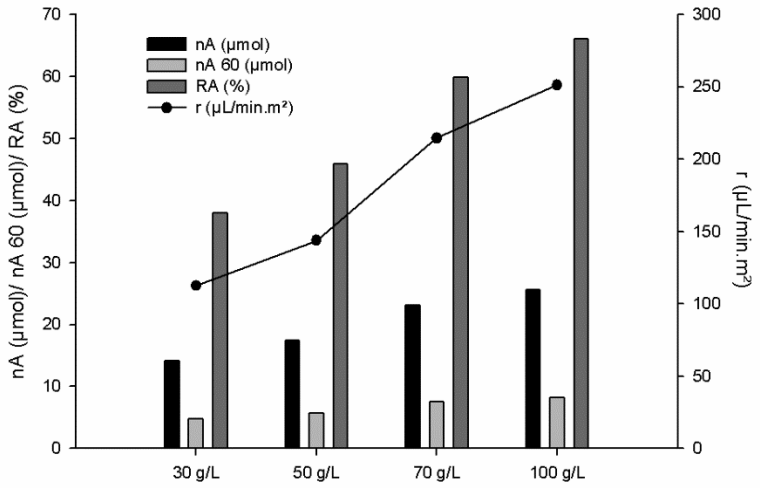


Figure 7: Quantitatively comparison of the photocatalytic activity of the coating.

Table 2 and Figure 7 show a quantitatively comparison of the photocatalytic activity for 4 different P25 loaded sol-gel coatings (30 g/L, 50 g/L, 50 g/L and 100 g/L). An obvious

conclusion is that the more P25 is added to the modified sol-gel, the more photocatalytic conversion is achieved according to all evaluating criteria (i.e. the removal percentage of acetaldehyde $R_A$, the quantity of acetaldehyde removed during the whole experiment *nA*, the quantity of acetaldehyde removed during the last hour of the experiment *nA(60)* and the photocatalytic rate per unit area *r*). Secondly, the quantity of acetaldehyde removed during the last hour nA(60) is for all P25 loadings more or less a third of the total quantity of acetaldehyde removed during the whole experiment of 3 hours. This indicates that the photocatalytic conversion is very stable from the moment that the UV-A light is switched on. Based on Figure 7, the 100 g/L P25 modified sol-gel coating performs best. We want to emphasize that in a realistic reactor geometry, several factors other than the coating activity may affect the efficiency and performance of the system. In the ISO standard reactor, light is uniformly distributed and the light irradiance is sufficient for the photocatalytic reaction to proceed. This may not be the case in a realistic setup.

## 4.3 Reactor performance

### 4.3.1 Light irradiance measurements

UV-A measurements were performed for all P25 loaded sol-gel coated 7ID9ED tubes in the multi-tube reactor and the results are given in Table 3. The UV-A (300-400 nm) light irradiance measured directly on the surface of the lamp was 12,000 µW/cm². At position 1 (Figure 4), located right behind the borosilicate reactor wall (> 95% UV-A transmission) at a distance of 5 mm, a UV-A light irradiance of 6,100 µW/cm² was measured. According to the results given in Table 3, a drastic reduction of light irradiance is observed from position 1 to position 2. Over 90% (for the highest P25 loaded coating even 99.5%) of the light did not pass the first coated tube. The light extinction is due to reflection, refraction and absorption and clearly depends on the amount of P25 used to prepare the coating. At position 4 (after 3 layers of tubes), the light emitted by the UV-A lamp is completely extinct for all coatings. The results indicate that light

transmission is an important design parameter and should be optimized to avoid 'dark spots'. The latter would permit harmful VOC molecules to pass through the reactor without being removed by photocatalysis. Even though the UV light drastically decreases while travelling through the solid parts of the reactor, a significant improvement can be made by appropriate and thoughtful design of both internal and external UV sources.

Table 3: UV-A measurements (300-400 nm) performed for all P25 loaded sol-gel coated 7ID9ED tubes at 4 fixed positions.

| Position | 0 g/L (µW/cm²) | 1 g/L (µW/cm²) | 5 g/L (µW/cm²) | 10 g/L (µW/cm²) | 30 g/L (µW/cm²) | 50 g/L (µW/cm²) | 70 g/L (µW/cm²) |
|---|---|---|---|---|---|---|---|
| 1 | 6100 (± 30) | 6,100 (± 30) | 6,100 (± 30) | 6,100 (± 30) | 6,100 (± 30) | 6,100 (± 30) | 6,100 (± 30) |
| 2 | 820 (± 11) | 642 (± 13) | 550 (± 12) | 500 (± 9) | 247 (± 2) | 84 (± 6) | 37 (± 2) |
| 3 | 240 (± 9) | 205 (± 5) | 150 (± 3) | 95 (± 2) | 22 (± 1) | 11 (± 1) | 6 (± 1) |
| 4 | 75 (± 3) | 57 (± 2) | 40 (± 1) | 23 (± 1) | 6 (± 1) | 3 (± 1) | 2 (± 1) |

4.3.2 Reactor performance at relatively low flow rates and high acetaldehyde concentrations

Figure 8 shows the acetaldehyde concentration profiles at the multi-tube reactor using online FTIR spectroscopy at a fixed flow rate of 500 mL/min during the four phases of the experiment (by-pass, adsorption, photocatalytic and second adsorption phase), for the multi-tube reactor built with 7ID9ED tubes. Similar experiments (at the same acetaldehyde inlet concentration) were performed for a flow rate of 1,500 mL/min (results not shown). The average acetaldehyde inlet concentration was derived from the by-pass phase for each experiment as $(2.19 \pm 0.05) \times 10^{-3}$ mol/m³. Variations of the inlet concentrations were due to the inaccuracy of the mass flow controllers.

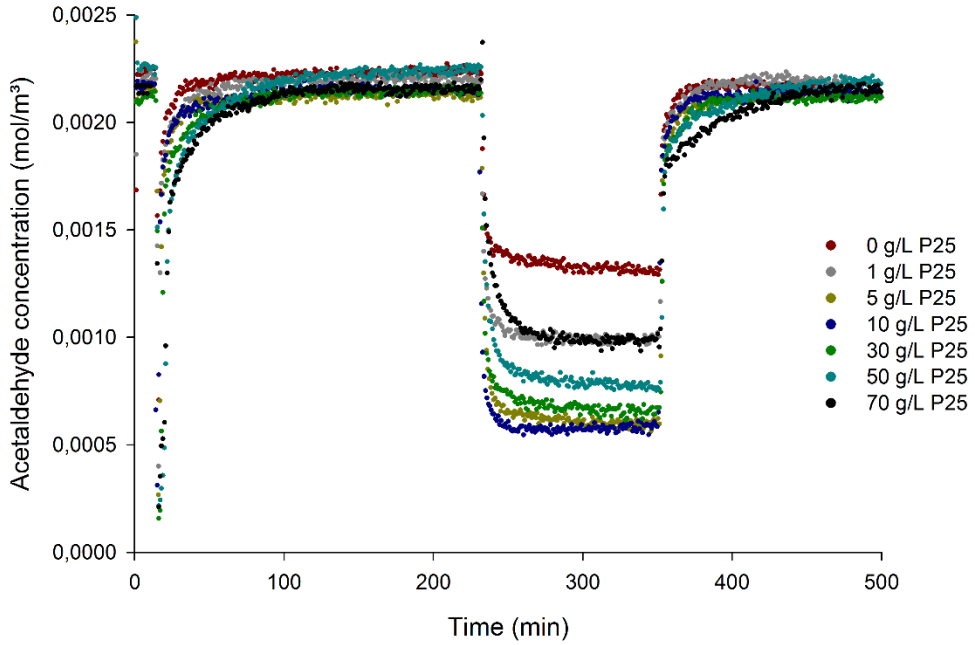


Figure 8: Acetaldehyde concentration profiles using online FTIR spectroscopy at a fixed flow rate of 500 mL/min.

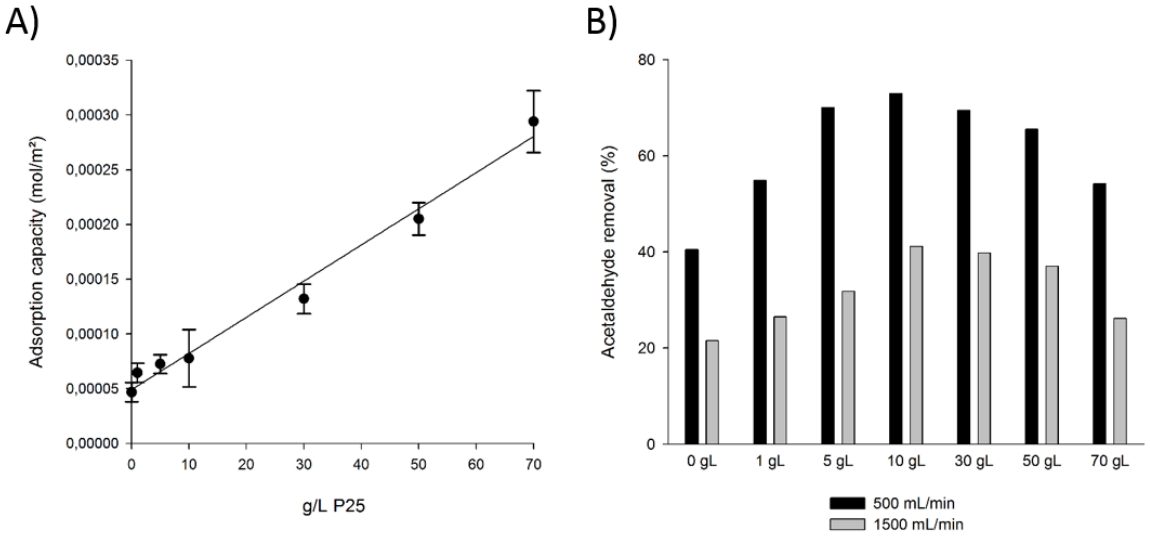


Figure 9: Characterization of different P25 loaded sol-gel coated multi-tube reactors: A) adsorption capacity (molm²); B) Acetaldehyde removal for two flow rates (%).

In Figure 9a, the adsorption capacity (an indication of the amount of active sites of the photocatalyst) for all coated set of tubes is shown. These values were derived by integrating the acetaldehyde concentration over time during the adsorption phase and subtracting the obtained values from the amount of acetaldehyde entering the reactor in during the same period, while

420 correcting for reactor dead space. The adsorption capacity of the coated tubes increased linearly
421 with the amount of P25 used to prepare the sol-gel ($R^2$=0.985). Figure 9b shows the
422 acetaldehyde removal capacity of the multi-tube reactor for both flow rates, 500 and 1,500
423 mL/min. Despite the high adsorption capacity of the 70 g/L sol-gel coating and despite the fact
424 that the photocatalytic reaction occurs from adsorbed acetaldehyde molecules, the highest
425 removal capacity was observed for the reactor containing 10 g/L P25 coated glass tubes. For
426 this coating, acetaldehyde removal capacity was 72.9 % and 41.1% for 500 and 1,500 mL/min
427 flow rate respectively. The adsorption and removal capacity of the 0 g/L P25 coated tubes can
428 be explained by the presence of titanium tetraisopropoxide in the sol-gel, which is a precursor
429 of titanium dioxide. The results are contrary to the previous findings (4.2.2 Photocatalytic
430 activity of the coating) where more P25 resulted in higher photocatalytic activity, even though
431 in the laboratory scale multi-tube reactor, two fluorescent UV-A lamps were used to illuminate
432 7 tubes. Clearly, the opposing effects of increasing the P25 load on the activity and the light
433 transmission should be accounted for in the design of an efficient PCO reactor, multi-tube
434 reactor or others and one should always compromise between photocatalytic activity and UV-
435 A light transmission.
436 4.3.3 Reactor performance at high flow rates and low acetaldehyde concentrations
437 For validation of the multi-tube reactor concept at more realistic HVAC operating conditions,
438 we tested the reactor with the three best performing coatings at the highest flow rate (10 g/L,
439 30 g/L and 50 g/L) at low acetaldehyde concentrations ($2 \times 10^{-4}$ mol/m³ as initial value)
440 combined with high flow velocities (2 - 2.5 m/s). Figure 10 shows the evolution of the
441 acetaldehyde concentration in the climate chamber, detected with the GC-FID. Considering the
442 duration of the experiments (about 10 hours), the conversion of acetaldehyde in low
443 concentration region is relatively similar for all tested coatings, which indicates mass-transfer
444 limited reaction kinetics as also reported in previous studies (Zhao and Yang 2003; Mamaghani

et al. 2017). Contrary to the results of the FTIR measurements (4.3.2), in this setup the 30 g/L coating performed better than the 10 g/L. The CADR calculation of the 10, 30 and 50 g/L multi-tube reactors resulted in 12.15, 13.73 and 10.48 respectively. Even though the initial concentration of acetaldehyde (5 ppmv) is about 10 times lower than the FTIR measurements, it still slightly exceeds realistic indoor VOC concentrations which are reported to be in the ppbv range (Hodgson et al. 2007; Kartheuser et al. 2012). The results prove the feasibility of the concept, but there is room for improvement toward reactor design and light configuration.

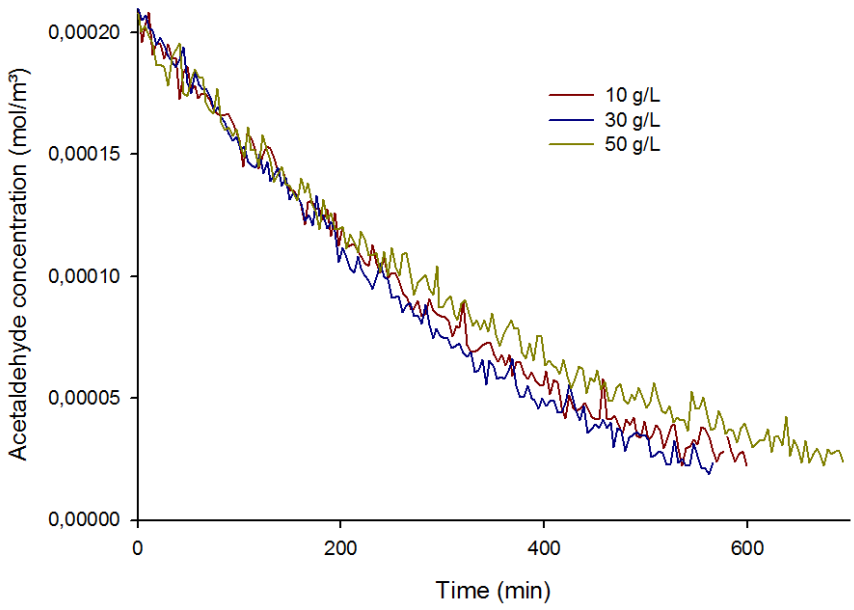


Figure 10: Acetaldehyde concentration profiles using GC-FID in an air-tight climate chamber

Different geometries and different light source configurations will result in a different choice of coating and therefore an in-depth case by case investigation is required in order to design, optimize and upscale multi-tube reactors for photocatalytic air purification. For this purpose, CFD and Multiphysics models such as the one used in 3.1.3 could be very helpful. An efficient reactor should have a high degradation efficiency, a high UV-A light transmission and a low pressure drop, in a physically compact vessel. For designing and optimizing PCO reactors (multi-tube reactors and other reactors) airflow dynamics models, light distribution models and

462 photocatalytic reaction kinetic models in a combined, so-called Multiphysics model, would
463 comprise a straightforward approach and tool for further design purposes.

## 464 5. Conclusions

465 A quantitative comparison of three potential glass substrates, based on the most vital selection
466 criteria for the operating conditions of a ventilation system, i.e. permeability and exposed
467 surface area, showed that glass tubes are the most promising substrate for photocatalytic air
468 purification reactors integrated in a ventilation system. Furthermore, a wide range of different
469 P25 loaded sol-gel coatings, suitable for glass substrates, were tested on coating adhesion and
470 activity properties. The higher the P25 in the sol-gel, the higher the photocatalytic activity; on
471 the other hand, a maximum of 50 g/L P25 could be added without loss of adhesion, according
472 to the classic scotch tape test. An in-depth characterization of the multi-tube reactor showed a
473 trade-off between photocatalytic activity and UV-A light transmission. These results indicate
474 reaction rate limited kinetics in the high concentration region at low flow rates and mass-
475 transfer limited kinetics in the lower concentration region at high flow rates. Since the operation
476 of reactors is based on complex interactive physical and chemical phenomena (air flow, mass
477 transfer via convection and diffusion, photocatalytic reactions and light distribution), it would
478 be useful to develop finite element models including all these phenomena as a tool for
479 designing, upscaling and optimizing these reactors.

## 480 6. Acknowledgement

481 J.V.W. acknowledges the Agentschap Innoveren & Ondernemen for a PhD fellowship.

## 482 7. References

483 Ao CHH, Lee SCC (2005) Indoor air purification by photocatalyst TiO2 immobilized on an activated
484 carbon filter installed in an air cleaner. Chem Eng Sci 60:103–109 . doi:

485 10.1016/j.ces.2004.01.073

486 Auvinen J, Ã LW (2008) The influence of photocatalytic interior paints on indoor air quality. Atmos
487 Environ 42:4101–4112 . doi: 10.1016/j.atmosenv.2008.01.031

488 Bejan A (2013) Convenction heat transfer. John Wiley & Sons, Inc, Hoboken, NJ, USA

489 Bourgeois P, Puzenat E, Peruchon L, et al (2012) Characterization of a new photocatalytic textile for
490 formaldehyde removal from indoor air. Appl Catal B Environ 128:171–178 . doi:
491 10.1016/j.apcatb.2012.03.033

492 Brosillon S, Lhomme L, Vallet C, et al (2008) Gas phase photocatalysis and liquid phase photocatalysis:
493 Interdependence and influence of substrate concentration and photon flow on degradation reaction
494 kinetics. Appl Catal B Environ 78:232–241 . doi: 10.1016/j.apcatb.2007.09.011

495 Çengel Y, Cimbala JM, Turner RH (2012) Fundamentals of Thermal-Fluid Sciences, Fourth ed. McGraw-
496 Hill, New York

497 Chen Y, Dionysiou DD (2008) Bimodal mesoporous TiO 2 – P25 composite thick films with high
498 photocatalytic activity and improved structural integrity. 80:147–155 . doi:
499 10.1016/j.apcatb.2007.11.010

500 Chen Y, Dionysiou DD (2007) A comparative study on physicochemical properties and photocatalytic
501 behavior of macroporous TiO 2 -P25 composite films and macroporous TiO 2 films coated on
502 stainless steel substrate. Appl Catal A 317:129–137 . doi: 10.1016/j.apcata.2006.10.025

503 Chen Y, Dionysiou DD (2006) TiO2 photocatalytic films on stainless steel: The role of Degussa P-25 in
504 modified sol-gel methods. Appl Catal B Environ 62:255–264 . doi: 10.1016/j.apcatb.2005.07.017

505 Claudio M, Andrea B, Marco M (2013) AC on the Standardization of the Photocatalytic Gas / Solid Tests.
506 Int J Chem React Eng 11:1–16 . doi: 10.1515/ijcre-2012-0045

507 Costarramone N, Kartheuser B, Pecheyran C, et al (2015) Efficiency and harmfulness of air-purifying
508 photocatalytic commercial devices: From standardized chamber tests to nanoparticles release.
509 Catal Today 252:6–11 . doi: 10.1016/j.cattod.2015.01.008

510 Destaillats H, Sleiman M, Sullivan DP, et al (2012) Applied Catalysis B : Environmental Key parameters
511 influencing the performance of photocatalytic oxidation ( PCO ) air purification under realistic
512 indoor conditions. Appl Catal B Environ 128:159–170 . doi: 10.1016/j.apcatb.2012.03.014

513 Hodgson AT, Destaillats H, Sullivan DP, Fisk WJ (2007) Performance of ultraviolet photocatalytic
514 oxidation for indoor air cleaning applications. Indoor Air 17:305–316 . doi: 10.1111/j.1600-

0668.2007.00479.x

Hossain M, Raupp GB, Hay SO, Obee TN (1999) Three-Dimensional Developing Flow Model for Photocatalytic Monolith Reactors. AICHE 45:

Kartheuser B, Costarramone N, Pigot T, Lacombe S (2012) NORMACAT project: normalized closed chamber tests for evaluation of photocatalytic VOC treatment in indoor air and formaldehyde determination. Environ Sci Pollut Res Int 19:3763–71 . doi: 10.1007/s11356-012-0797-0

Mamaghani AH, Haghighat F, Lee CS (2017) Photocatalytic oxidation technology for indoor environment air purification: The state-of-the-art. Appl Catal B Environ 203:247–269 . doi: 10.1016/j.apcatb.2016.10.037

Mills A, Hill C, Robertson PKJ (2012) Journal of Photochemistry and Photobiology A : Chemistry Overview of the current ISO tests for photocatalytic materials. J Photochem Photobiol A Chem 237:7–23 . doi: 10.1016/j.jphotochem.2012.02.024

Mills A, Hunte S Le (2000) An overview of semiconductor photocatalysis. J Photochem Photobiol A 108:1–35

Mo J, Zhang Y, Xu Q, et al (2009a) Determination and risk assessment of by-products resulting from photocatalytic oxidation of toluene. Appl Catal B Environ 89:570–576 . doi: 10.1016/j.apcatb.2009.01.015

Mo J, Zhang Y, Xu Q, et al (2009b) Photocatalytic purification of volatile organic compounds in indoor air: A literature review. Atmos. Environ. 43:2229–2246

Paz Y (2010) Application of TiO2 photocatalysis for air treatment: Patents' overview. Appl Catal B Environ 99:448–460

Sanchez B, Sanchez-Munoz M, Munoz-Vicente M, et al (2012) Photocatalytic elimination of indoor air biological and chemical pollution in realistic conditions. Chemosphere 87:625–630 . doi: 10.1016/j.chemosphere.2012.01.050

Sleiman M, Conchon P, Ferronato C, Chovelon J-M (2009) Photocatalytic oxidation of toluene at indoor air levels (ppbv): Towards a better assessment of conversion, reaction intermediates and mineralization. Appl Catal B Environ 86:159–165 . doi: 10.1016/j.apcatb.2008.08.003

Sopyan I, Watanabe M, Murasawa S, et al (1996) An efficient TiO2 thin-film photocatalyst : photocatalytic properties in gas-phase acetaldehyde degradation. J Photochem Photobiol A 98:79–86

Sun R, Nakajima A, Watanabe I (2000) TiO2 -coated optical fiber bundles used as a photocatalytic filter for decomposition of gaseous organic compounds. J Photochem Photobiol A Chem 136:111–116

Tytgat T, Hauchecorne B, Smits M, et al (2012) Concept and Validation of a Fully Automated Photocatalytic Test Setup. J Lab Autom 17: . doi: 10.1177/2211068211424554

van Walsem J, Verbruggen SW, Modde B, et al (2016) CFD investigation of a multi-tube photocatalytic reactor in non-steady- state conditions. Chem Eng J 304:808–816 . doi: 10.1016/j.cej.2016.07.028

Verbruggen SW, Keulemans M, van Walsem J, et al (2016) CFD modeling of transient adsorption/desorption behavior in a gas phase photocatalytic fiber reactor. Chem Eng J 292:42–50 . doi: 10.1016/j.cej.2016.02.014

Verbruggen SW, Masschaele K, Moortgat E, et al (2012) Factors driving the activity of commercial titanium dioxide powders towards gas phase photocatalytic oxidation of acetaldehyde. Catal Sci Technol 2:2311–2318 . doi: doi: 10.1039/C2CY20123B

Verbruggen SW, Ribbens S, Tytgat T, et al (2011) The benefit of glass bead supports for efficient gas phase photocatalysis : Case study of a commercial and a synthesised photocatalyst. Chem Eng J 174:318–325 . doi: 10.1016/j.cej.2011.09.038

Wang K, Tsai H, Hsieh Y (1998) The kinetics of photocatalytic degradation of trichloroethylene in gas phase over TiO 2 supported on glass bead. Appl Catal B Environ 17:313–320

Yu QL, Brouwers HJH (2009) Environmental Indoor air purification using heterogeneous photocatalytic oxidation. Part I: Experimental study. Appl Catal B Environ 92:454–461 . doi: 10.1016/j.apcatb.2009.09.004

Zhang Y, Yang R, Zhao R (2003) A model for analyzing the performance of photocatalytic air cleaner in removing volatile organic compounds. Atmos Environ 37:3395–3399 . doi: 10.1016/S1352-2310(03)00357-1

Zhao J, Yang X (2003) Photocatalytic oxidation for indoor air purification: a literature review. Build Environ 38:645–654 . doi: 10.1016/S0360-1323(02)00212-3

Zhong L, Haghighat F (2015) Photocatalytic air cleaners and materials technologies – Abilities and limitations. Build Environ 91:191–203 . doi: 10.1016/j.buildenv.2015.01.033